ACS APPLIED MATERIALS & INTERFACES

www.acsami.org

Research Article

Temperature-Dependent Morphological Evolution during Corrosion of the Ni-20Cr Alloy in Molten Salt Revealed by Multiscale Imaging

Xiaoyang Liu, Kaustubh Bawane, Xiaoyin Zheng, Mingyuan Ge, Phillip Halstenberg, Dmitry S. Maltsev, Alexander S. Ivanov, Sheng Dai, Xianghui Xiao, Wah-Keat Lee, Lingfeng He, and Yu-chen Karen Chen-Wiegart*

Cite This: *ACS Appl. Mater. Interfaces* 2023, 15, 13772−13782

Read Online

ACCESS | Metrics & More | Article Recommendations | Supporting Information

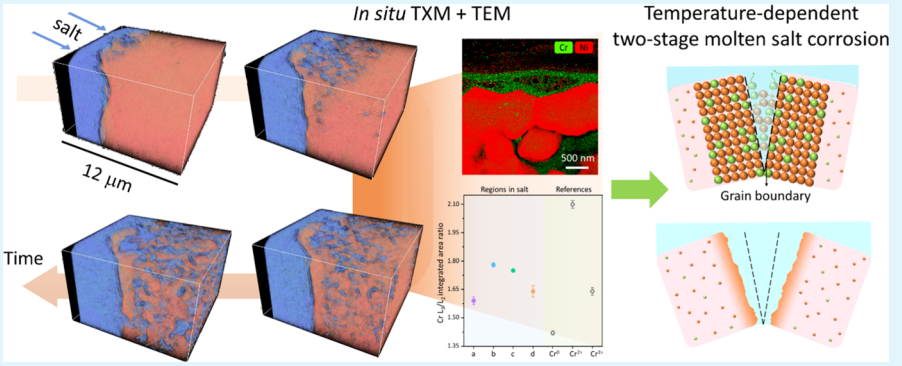

ABSTRACT: Understanding the mechanisms leading to the degradation of alloys in molten salts at elevated temperatures is significant for developing several key energy generation and storage technologies, including concentrated solar and next-generation nuclear power plants. Specifically, the fundamental mechanisms of different types of corrosion leading to various morphological evolution characteristics for changing reaction conditions between the molten salt and alloy remain unclear. In this work, the three-dimensional (3D) morphological evolution of Ni−20Cr in KCl−$MgCl_2$ is studied at 600 °C by combining in situ synchrotron X-ray and electron microscopy techniques. By further comparing different morphology evolution characteristics in the temperature range of 500−800 °C, the relative rates between diffusion and reaction at the salt−metal interface lead to different morphological evolution pathways, including intergranular corrosion and percolation dealloying. In this work, the temperature-dependent mechanisms of the interactions between metals and molten salts are discussed, providing insights for predicting molten salt corrosion in real-world applications.

KEYWORDS: *dealloying, physical and chemical properties, molten chloride salt, Ni-based alloy, high-temperature corrosion*

1. INTRODUCTION

Understanding material degradation in molten salt environments is instrumental for developing sustainable energy systems, such as next-generation nuclear reactors and large-scale concentrated solar thermal power plants. In the nuclear energy cycle, molten salts are used as electrolytes for electrochemical separation of used nuclear fuel and as heat transfer fluids in molten salt cooled/fueled nuclear reactors.[1] Specifically, molten salts are attractive as coolants because of their high volumetric heat capacities and boiling points, allowing for high operating temperatures (reaching 700−750 °C) and near atmospheric pressure relative to light water reactors.[2] Thus, a molten salt reactor (MSR) is considered a safer, more efficient, and sustainable design for nuclear power plants. However, structural materials may degrade in a molten salt environment due to the selective dissolution of alloy elements and the lack of oxide-based passivation protection.[3] It is of critical importance to mechanistically understand the nature of corrosion and its corresponding microstructural changes in materials to prevent these detrimental issues.

The electrochemical dissolution of Cr, which is the most susceptible alloying element, occurs in molten chloride salts in Fe- or Ni-based alloys. This corrosion is caused by inevitable contamination (H_2O and O_2) and the strongly hygroscopic nature of salts, such as $ZnCl_2$ and $MgCl_2$.[4−7] The wide range of molten salt and alloy systems, coupled with complex factors, including temperature, radiation effect, and addition of metal

Received: December 28, 2022
Accepted: February 21, 2023
Published: March 6, 2023

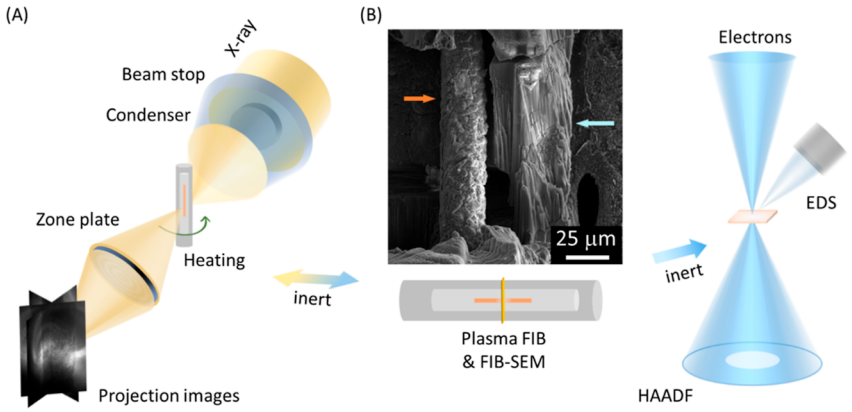

Figure 1. Experimental setup and sample transfer method of multimodal in situ synchrotron TXM and TEM. (A) In situ TXM setup. (B) Post-TXM analysis, the sample was first prepared with Xe ions in a PFIB system and then Ga ions in a focused ion beam SEM (FIB-SEM) system. The extracted thin sample was then analyzed by STEM with EDS and EELS. The inert experimental environment was kept throughout the workflow to avoid exposing the sample to air or moisture. The orange arrow shows the corroded wire with salt, and the blue arrow shows the quartz capillary in PFIB prior to extracting the sample section for STEM analysis.

ions including fission products and corrosion products from structural alloys, further complicate the corrosion of alloys, leading to different morphologies and corrosion rates.[3,5,8−10] The variations in these parameters change the interplay between the chemical/electrochemical reactions and the mass transport processes, including interfacial diffusion at the salt−metal interface and long-range diffusion in the molten salts and bulk alloys, manifesting as different kinetic phenomena. Temperature plays a key role among the different parameters that affect molten salt corrosion. It directly influences the kinetics of the competing chemical reactions and diffusion events, and wide temperature differentials exist between different sections of molten salt reactors and concentrated solar power plants.[1,5,11,12]

Although different porous morphologies at various temperatures of Ni-based alloys have been observed experimentally,[6,13−15] the mechanistic understanding of morphological evolution as a function of temperature has not been discussed in depth, in part due to the challenges in directly imaging and quantifying the morphological changes in these systems at elevated temperatures under controlled conditions. Recent works have utilized synchrotron X-ray nanotomography to enable direct observation of the 3D morphological evolution characteristics of alloys in molten salts[16] and multimodal imaging techniques that combine X-ray and electron microscopy analyses to understand the morphological changes from the nano- to microscales.[17,18]

In this work, a Ni−20Cr alloy corroding in molten KCl−$MgCl_2$ (50−50 mol %) at 600 °C was studied by in situ synchrotron X-ray nanotomography with transmission X-ray microscopy (TXM). Subsequently, the in situ sample was preserved without air and moisture exposure and analyzed by scanning transmission electron microscopy (STEM) coupled with energy-dispersive X-ray spectroscopy (EDS) and electron energy loss spectroscopy (EELS). The underlying mechanism for the corrosion morphology that forms at 600 °C is discussed. In addition, the effects of temperature (500,[19] 600, 700, and 800 °C[16]) on the interfacial behaviors are discussed in this study, resulting in different morphological evolution characteristics. Overall, in-depth insights into the corrosion mechanisms in a molten chloride salt with the effects of temperature are provided in this work. In agreement with previous studies from a thermodynamic point of view, the importance of kinetic effects on molten salt corrosion is suggested in this study, including the relative rates of surface diffusion and reaction at the salt−metal interface.

2. METHODS

2.1. In Situ Synchrotron TXM Sample Preparation, Characterization, and Data Processing. The KCl−$MgCl_2$ (50−50 mol %) salt was purified and mixed following salt purification as detailed in previous work.[17,9,20−22] An as-drawn Ni−20Cr microwire with a diameter of 20 μm and a composition of 80 wt % Ni and 20 wt % Cr (99.5% pure, Goodfellow, USA-NI055105) was used in this study. The wire was placed in an open-ended quartz capillary with a diameter of 0.1 mm (Charles Supper), which was first heated to remove adsorbed organic matter and water. The sample was baked in an oven (CASCADE TEK) at 120 °C overnight to remove surface moisture and then transferred into an argon-filled glovebox. Inside the glovebox, the KCl−$MgCl_2$ salt mixture was melted at ∼550 °C in a quartz boat. The molten salt was drawn into a wire-filled capillary by a syringe attached to the funnel end of the capillary and rapidly solidified. Subsequently, the capillary with the wire was placed in a closed-end capillary with a diameter of 0.3 mm. The funnel side of the large capillary was sealed with epoxy and cured overnight in a glovebox. Finally, the sample was removed from the glovebox and immediately flame-sealed using a miniature benchtop hydrogen torch (Rio Grande).

The sealed double-capillary sample was measured by in situ X-ray nanotomography at the full-field X-ray imaging beamline (FXI; 18-ID)[23] equipped with a miniature furnace[24] at National Synchrotron Light Source II (NSLS-II) of the Brookhaven National Laboratory (Figure 1A). The sample was heated to 600 °C at a ramp rate of 25 °C/min. The energy for the incident X-ray was 8.33 keV, and the size of the field of view was 51.2 × 43.2 μm^2 with an effective pixel size of 40.0 nm by camera binning of 2 × 2. The reported optical resolution of the TXM at the FXI beamline was sub-50 nm for rapid 3D nanotomography.[23] After the sample cooled down to room temperature, 2D X-ray absorption near-edge spectroscopy (XANES) images of the sample were obtained across the Ni K-edge. Standard spectroscopic images from a Ni foil were also collected for energy calibration. The XANES data were processed using PyXAS and Athena software.[25,26]

The captured in situ tomography projection images were low-pass-filtered with the gridrec algorithm and reconstructed with Tomopy.[27,28] Then, the 3D tomographic reconstruction stack images were cropped to 27.4 × 27.4 × 12.0 μm^3, aligned using Dragonfly software (2020.1, Object Research Systems Inc.), and visualized by Avizo software (Thermo Fisher Scientific, v.9.3). The 12 μm dimension was along the length of the wire, defined as the z direction

https://doi.org/10.1021/acsami.2c23207
ACS Appl. Mater. Interfaces 2023, 15, 13772−13782

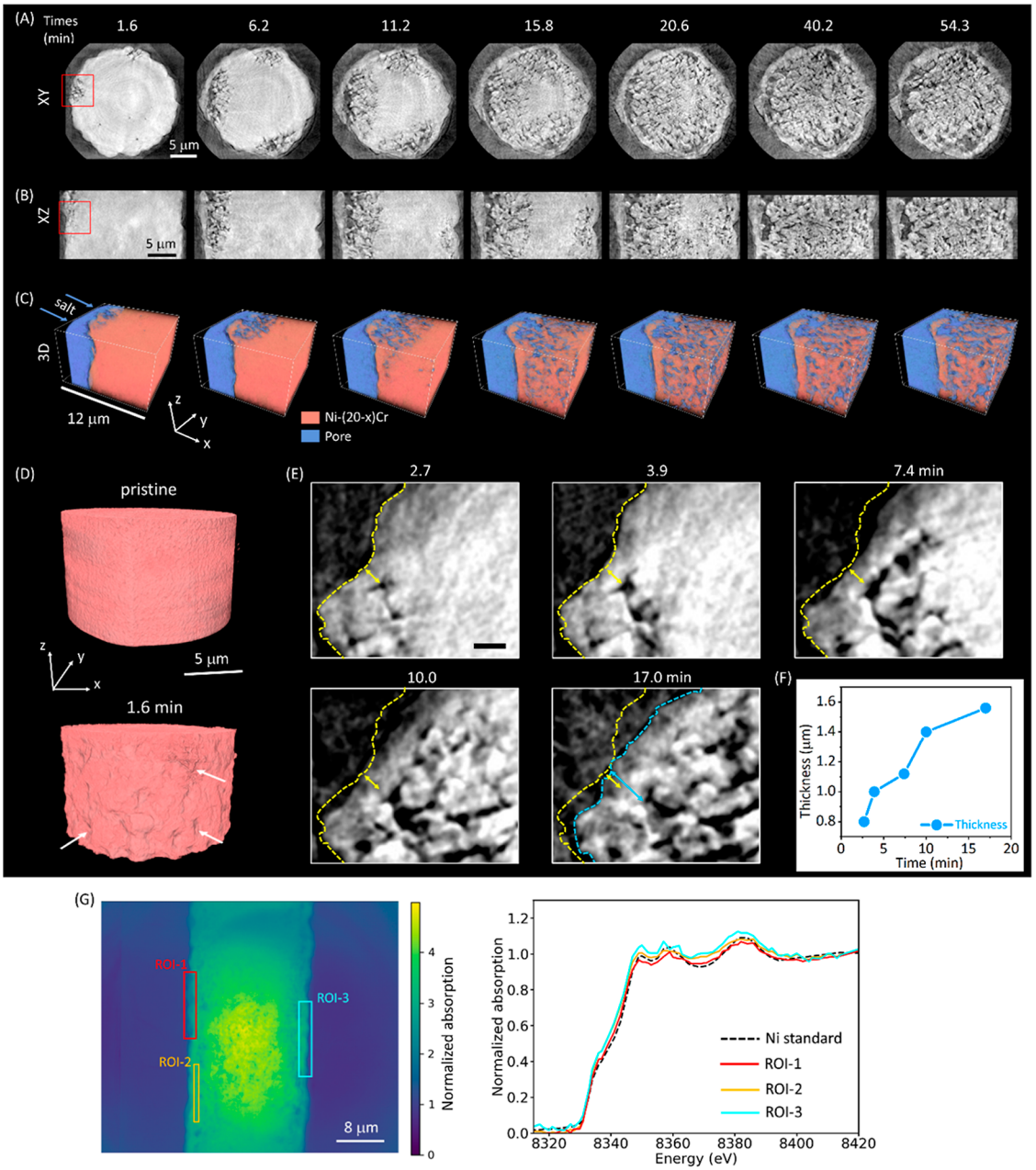

Figure 2. Morphological evolution of Ni−20Cr in KCl−$MgCl_2$ at 600 °C. (A−B) 2D (XY and XZ) pseudo-cross-sectional views of the Ni−20Cr morphologies at different time points. (C) 3D morphological evolution of the region highlighted by a red rectangle in (A−B). (D) Surface morphologies of the pristine Ni−20Cr wire at room temperature and after reacting in molten salt at 600 °C for 1.6 min. The surface reacted and roughened quickly after corroding by molten KCl−$MgCl_2$ (indicated by white arrows). (E) Evolution of the surface layer with the reaction time. The scale bar is 1 μm. The yellow dashed line is the surface profile of the corroded sample at 2.7 min, and the yellow arrow indicates the thickness. The blue dashed line is the surface profile at 17.0 min, which is smoother than the yellow dashed line. The blue arrow shows the thickness at 17.0 min, which exceeds the yellow arrow corresponding to the initial thickness at 2.7 min. (F) Plot showing that the thickness of the surface layer increased with the reaction time, as calculated from the position indicated in Figure S3. (G) Representative frame from the 2D XANES spectroscopic imaging with three ROIs on the surface layer with their normalized Ni K-edge XANES spectra. The measurement was conducted on the sample after it was cooled down to room temperature.

in the reconstructed data. In addition, to segment the 3D reconstructed images, the Trainable Weka segmentation in freeware ImageJ,[29] a machine learning method, was applied to segment Ni−20Cr and the nonmetal phases (the exterior region and interior pores) as the initially segmented images. However, the interior pores within the Ni−20C wire and the exterior of the sample (background) had similar X-ray attenuation levels. To segment these two phases, a mask of the sample region was created as follows. The initially segmented images were projected and summed over the z direction (the length of the wire direction); a threshold value was chosen to identify the border of the Ni−20Cr wire. A void-filling algorithm using the SciPy package[30] was applied to fill the interior pores to create a mask corresponding to the sample region. The mask image was then applied to the initially segmented images to identify the exterior background. The image segmentation workflow is shown in Figure S1.

2.2. TEM/STEM Sample Preparation and Characterization. The inner capillary containing the Ni−20Cr microwire corroded in situ at the synchrotron was carefully recovered and placed on a scanning electron microscopy (SEM) stub by breaking the outer capillary inside an inert-atmosphere glovebox. The inner capillary was

https://doi.org/10.1021/acsami.2c23207
ACS Appl. Mater. Interfaces 2023, 15, 13772−13782

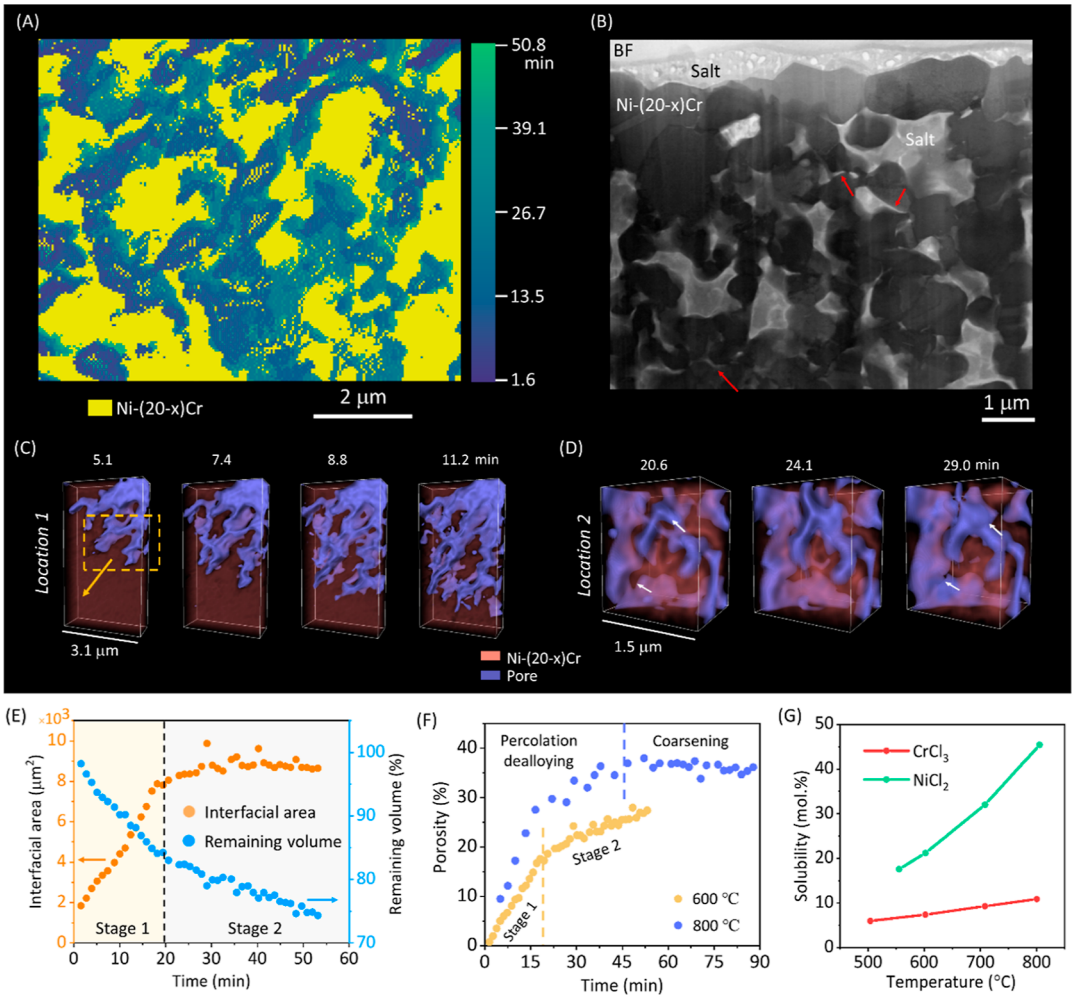

Figure 3. Synchrotron X-ray nanotomography and STEM−BF imaging showing two-stage corrosion at 600 °C. (A) A 2D colormap shows the pore evolution along with reaction time in one pseudo-cross-sectional view from the X-ray nanotomography (XY). The remaining Ni-(20-*x*)Cr after the reaction is shown in yellow. The color transition from blue to green shows the time points when the alloy dissolved. (B) STEM−BF image of the sample after the in situ experiment shows the pores from intergranular corrosion. (C) Location 1: A local 3D view shows the progression of intergranular corrosion during corrosion stage 1. The yellow arrow indicates the direction along which corrosion progressed. (D) Location 2: The intergranular pores progressed from corrosion attacking the grain surface during corrosion stage 2. The white arrows show where surface corrosion occurred. (E) Interfacial area and volume change in the Ni−20Cr wire as a function of reaction time in molten KCl−$MgCl_2$ in the two-stage reaction separated by a dashed line. (F) Porosity evolution comparison between 600 (stages 1 and 2, separated by a yellow dashed line) and 800 °C (percolation dealloying and coarsening, separated by a purple dashed line).[16] (G) Solubilities of $NiCl_2$ and $CrCl_3$ increase with increasing temperature in molten KCl−$MgCl_2$ (50−50 mol %).

transferred to a plasma-focused ion beam (PFIB; Thermo Scientific) system attached to an inert-atmosphere glovebox for air-free sample preparation. Roughly, an ∼100 μm length of the Ni−20Cr microwire was exposed by carefully milling the inner capillary using a Xe ion beam and lifting a window from the capillary (Figure 1B). The capillary with the exposed window was transferred to a FIB system for TEM lamella preparation using a Ga ion beam. The TEM lamella mounted on a Cu half-grid in a stainless-steel, argon-filled can were transferred to an inert-atmosphere glove bag (Erlab portable glove bag), loaded on a vacuum transfer TEM sample holder (Gatan), and then immediately inserted into the Titan Themis 200 TEM system (Thermo Scientific) for characterization. Microstructure, elemental distribution, and oxidation state analyses at salt−alloy interfacial regions of the corroded Ni−20Cr sample were performed using STEM equipped with Super X EDS and Continuum ER EELS (Gatan) systems. A step size of 2.91 nm was used in the STEM/EDS mapping.

2.3. Solubility Measurement. The solubilities of anhydrous $CrCl_3$ and $NiCl_2$ (99.99% purity, Aldrich-APL) in the molten KCl−$MgCl_2$ salt mixture were measured at 500−800 °C using the isothermal saturation method reported previously.[16]

3. RESULTS AND DISCUSSION

3.1. In Situ 3D Morphological Evolution at 600 °C. The 2D XY and XZ pseudocross-sectional views and 3D morphological changes in the Ni−20Cr microwire at different reaction times in molten KCl−$MgCl_2$ (50−50 mol %) at 600 °C are shown in Figure 2A−C (Videos S1 and S2). Corrosion occurred on the sample, forming pores from the surface to the center with increasing reaction time. Large pores developed in the corroded sample at longer times. When comparing the surface of the pristine wire measured at room temperature and after reacting in the molten salt for 1.6 min (Figure 2D), it was obvious that at the onset of the metal−salt interfacial reaction, the surface of the Ni−20Cr wire reacted with the molten salt, creating defects. Note that the initiation of the pores occurred at specific locations, and future work can be carried out to

https://doi.org/10.1021/acsami.2c23207
ACS Appl. Mater. Interfaces 2023, 15, 13772−13782

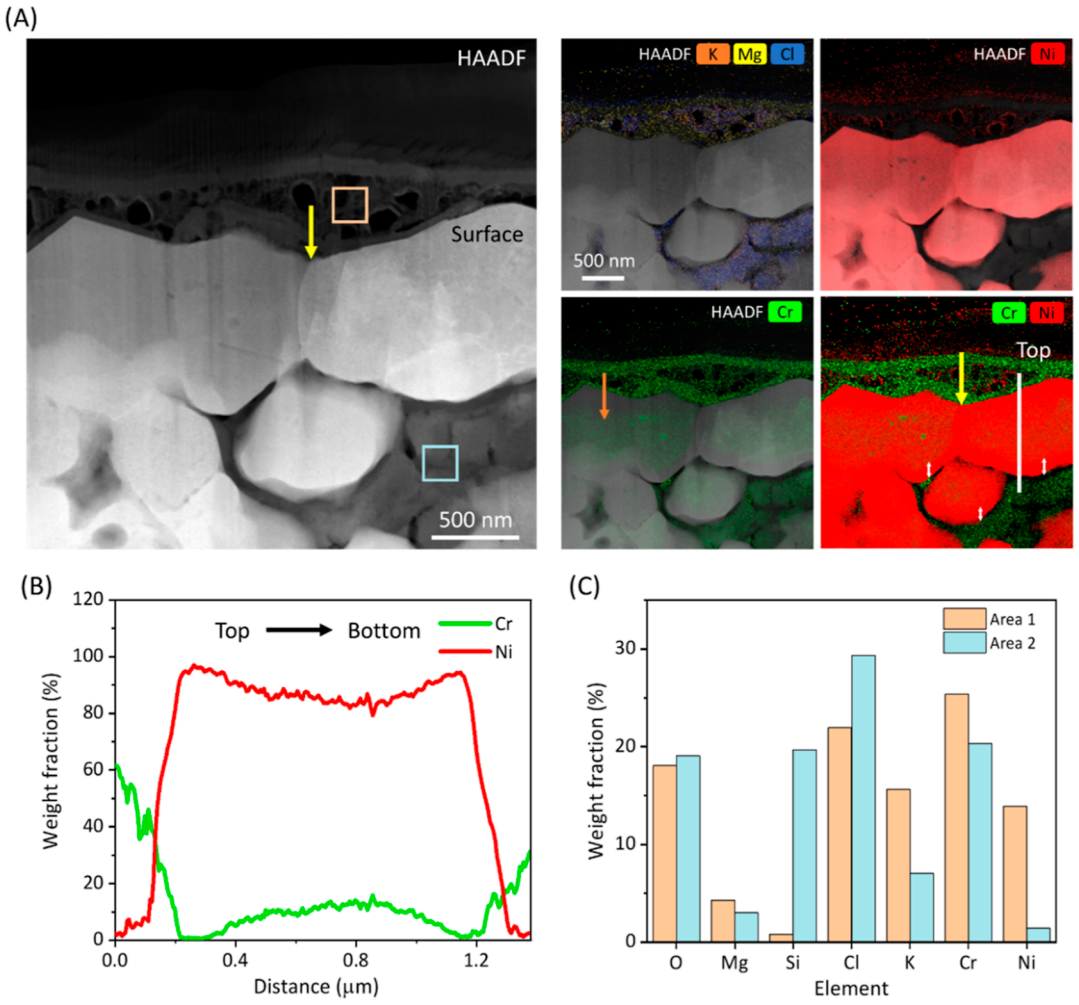

Figure 4. STEM analysis of Ni−20Cr after corrosion in molten salt without exposure to air showing the elemental distributions in both the alloy and the salt. (A) High-angle annular dark-field image by STEM shows the alloy (bright) and remnant salt (dark) filled in pores and attached to the alloy surface from the image contrast. EDS analysis shows the elemental distributions of salt elements (K, Mg, and Cl) and alloying elements (Ni and Cr). The region between the two grains (highlighted by a yellow arrow) was depleted of Cr and enriched with Ni. The grain surface (~tens of nanometer) was Ni-rich (white double-sided arrows). The center of the grain contained Cr (orange arrow). (B) Weight ratio evolution characteristics of Ni and Cr along the white line in (A) from top to bottom shows a Ni-rich surface and Ni−20Cr center. (C) Weight ratios of different elements in the salt regions, as indicated by the light-orange square (area 1) and light-blue rectangles (area 2) in (A).

further investigate the onset of corrosion at the metal−salt interface. The degradation of Ni−20Cr occurred due to the preferential dissolution of Cr because the redox potentials of Cr(II)/Cr and Cr(III)/Cr are lower than those of Ni(II)/Ni in molten chloride salt.[1,31] Interestingly, the sample surface morphology changed with the reaction time.

A local change is shown in Figure 2E, Figure S2, and Video S3. As shown in Figure 2E, the surface was rough with concave and convex features at 2.7 and 3.9 min, which were the results of corrosion. However, after 3.9 min, the surface gradually flattened. Moreover, the thickness of the surface layer increased from 0.8 to 1.6 μm with the reaction time (Figures 2E and S3). The surface flattening and thickness change resulted from a surface smoothing and coarsening effect, driven by minimizing the total surface energy.[32] These processes were likely created by the surface diffusion of Ni after Cr dissolution, rearranging the surface morphology to decrease the interfacial area and therefore decrease the interfacial surface energy. Both changes were obvious from 2.7 to 3.9 min, suggesting that the surface diffusion of Ni was fast in molten KCl−$MgCl_2$; these results are consistent with prior observations of pure Ni particle growth in the same type of salt.[33] A competing hypothesis was that the growth of this layer came from a redeposition of either Ni reduction in Ni or Ni oxides or chlorides. However, as shown in Figure 2G, the XANES spectra of the region of interest (ROI-1,2,3) in the surface layer were consistent with the one from the metallic Ni standard and not Ni oxides or chlorides. Moreover, the STEM/EDS analysis discussed in the following section showed that there was very little Ni dissolution, making the redeposition of pure Ni unlikely. Thus, the results are not consistent with the second hypothesis. Since 2D XANES integrates the chemical information along the X-ray beam path, to further probe the Ni chemical states at the surface in nanoscale, 3D XANES imaging,[34] soft X-ray absorption spectroscopy in total electron yield or fluorescence yield[35,36] modes can be applied in the future to potentially capture any surface chemical species that could play a role in the reaction between the liquid and solid phases.

The propagation of the pores in the corroded sample was further studied in detail. Figure 3A shows the evolution of pores with increasing reaction time in one pseudo-cross-

https://doi.org/10.1021/acsami.2c23207
ACS Appl. Mater. Interfaces 2023, 15, 13772−13782

sectional XY view extracted from Figure S4. The yellow color represents the remaining Ni-(20-x)Cr phase. The color scale from light blue to green corresponds to the time points when the corrosion occurred at a specific location, creating porosity in the initial alloy. For most of the pores, a color transition from light blue to green was observed from the center to the interface between the pore and Ni-(20-x)Cr phase. This result suggests that after the initial corrosion formed the pores from the surface to the center of the Ni−20Cr wire, Cr dissolution occurred at the interface between molten salt and Ni-(20-x)Cr over an extended period of reaction. Thus, a two-stage corrosion process was observed in this work: stage 1: intergranular corrosion along grain boundaries (as shown in the Supporting Information, Video S4) and stage 2: corrosion into the grain surface next to grain boundaries (Video S5).

Correspondingly, STEM analysis of the corroded sample after the in situ experiment shows that the pores were mostly developed throughout grain boundaries, suggesting intergranular corrosion (Figure 3B, red arrows). Furthermore, the two-stage morphological changes at two locations (Figure S5) in the sample are shown in Figure 3C−D. For location 1, at 5.1 min, the pores emerged. With increasing reaction time, corrosion progressed along grain boundaries without attacking the material in other directions than grain boundaries until 12.4 min, corresponding to stage 1. For location 2 at 20.6 min, intergranular pores were observed. With a longer reaction time, the intergranular pores increased in width (indicated by white arrows) from the corrosion into the surfaces of adjacent grains, corresponding to stage 2.

To quantify this two-stage morphological change behavior, the volume and interfacial area changes based on the 3D X-ray tomography data were calculated (Figure 3E). From the beginning of the reaction until ∼20.6 min (stage 1), a rapid decrease in the volume with increasing interfacial area resulted from intergranular corrosion. The atomic structures at grain boundaries were more disordered and thus possessed a higher free energy relative to that in the bulk lattices; the atoms in grain boundaries could then be dissolved more easily,[19,37] thereby promoting corrosion attack.[32,38]

Subsequently, the volume of the Ni−20Cr alloy decreased at a slow rate (stage 2), while the interfacial area did not show an evident change. During stage 2, corrosion occurred at grain surfaces without creating intragranular pores; this surface corrosion was slower than intergranular corrosion. Note that the complete dissolution of some grains was observed from the TXM and STEM−BF images. Additionally, Figure 3F shows a comparison of porosity evolution at 600 and 800 °C.[16] At the same reaction time (∼53.2 min), the porosity at 600 °C was ∼10% lower than that at 800 °C, suggesting less serious corrosion at 600 °C. Moreover, the porosity change rate was calculated (Figure S6). The porosity change rate at 800 °C during percolation dealloying (until ∼47.0 min) was in the range of 2−6%; it was mostly below 2% at 600 °C during intergranular corrosion. The intergranular corrosion rate at 600 °C was slower than the percolation dealloying rate at 800 °C.

Finally, the solubilities of $CrCl_3$ and $NiCl_2$ in molten KCl−$MgCl_2$ (50−50 mol %) as functions of temperature are shown in Figure 3G and Table S1. The solubilities of these potential corrosion products increased with temperature. Overall, the solubility of $CrCl_3$ is lower than that of $NiCl_2$ throughout the temperature range from ∼500 to 800 °C. The solubility of $CrCl_3$ in molten KCl−$MgCl_2$ (50−50 mol %) showed an ∼5 mol % difference between 555 and 805 °C. With relatively lower solubilities at 500 and 600 °C, Cr-containing species could precipitate at the interfaces, thus changing the interaction between the original KCl−$MgCl_2$ and its alloy. Thermodynamically, the redox potential of the Cr anodic reaction is related to the concentration of Cr^{3+} at the interface according to the Nernst equation.[1] The solubilities of ions in molten salt versus temperature are important considerations for molten salt applications with temperature differences between the hot and cold legs of a circulating system, causing thermal gradient-driven corrosion.[39]

3.2. Post-Corrosion Chemical Analysis of the Alloy and Salt Specimen. After in situ corrosion, the intact, salt-encrusted Ni−20Cr wire was characterized by high-resolution STEM without exposure to air; thus, the chemical states of the corrosion products were preserved. The remaining salt was identified above the surface and in the pores of the corroded Ni-(20-x)Cr wire from the image contrast and the salt elemental distribution−K, Mg, and Cl (Figures 4A and S7); these findings are consistent with the morphology observed by in situ synchrotron X-ray nanotomography. In addition, the distributions of Ni (red) and Cr (green) on corroded Ni-(20-x)Cr are shown in Figure 4A. Between two grains (highlighted by a yellow arrow), the figure shows the depletion of Cr and enrichment of Ni.

The grain surface barely contains Cr (shown as Ni-rich), while the grain interior still contained high levels of Cr. The weight fraction gradation of Ni and Cr from the grain interior to the grain surface (Figure 4A, white line) was quantified in Figure 4C. The surface layer of the grain showed ∼100 wt % Ni with a thickness on the order of tens of nanometers. The center of the grain was composed of ∼80 wt % Ni and 20 wt % Cr, which was similar to the composition of the parent Ni−20Cr. Thus, during corrosion, Cr developed a concentration gradient from the center to the surface of the grain, providing a possibility for Cr lattice diffusion at 600 °C. Chen and Sieradzki[40] summarized that lattice diffusion supported dealloying, forming a negative void dendrite morphology. Because no pores formed within the grain, the lattice diffusion of Cr did not support the formation of pores through dealloying in this case.

The weight fractions of the elements in the salt regions (marked by light-orange and blue frames in Figure 4A) are shown in Figure 4C. In the remnant salt, although Cr and Ni were present, there was a higher weight ratio of Cr compared to Ni, suggesting that major corrosion occurred for Cr. Accordingly, the redox potentials of $Cr/CrCl_2$ and $Cr/CrCl_3$ are more negative than those of $Ni/NiCl_2$; thus, Cr is more easily oxidized than Ni in this region.[1] After the selective reaction of Cr, Ni atoms were left on the grain boundaries. The remaining Ni atoms could attach or diffuse to an adjacent grain surface. We detected a lower amount of Ni (13.9 wt % in area 1; 1.4 wt % in area 2) in the remnant salt, suggesting that most Ni atoms were not dissolved but preferred to merge with the adjacent grain surface. These findings are similar to those from quasi-in situ TEM,[19] which observed that Ni-rich and Cr-depleted particles formed and detached at the tips and edges of the intergranular cracks formed at the early stages of the intergranular corrosion of Ni−20Cr. The impact of Ni attachment to the grain surfaces on molten salt corrosion is further discussed in the next Section 3.3.

Finally, Figures 4C and S8 show the presence of Si and O in the sample. The Si could be from the quartz capillary, indicating that molten KCl−$MgCl_2$ could degrade the quartz;

https://doi.org/10.1021/acsami.2c23207
ACS Appl. Mater. Interfaces 2023, 15, 13772−13782

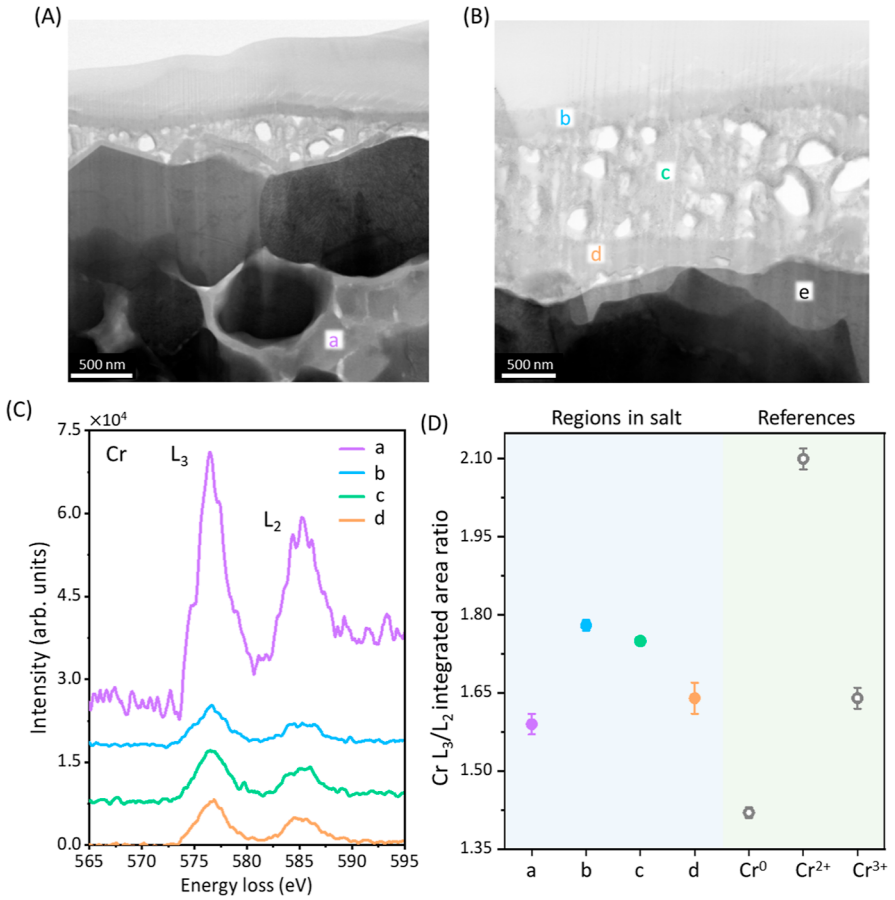

Figure 5. EELS analysis determined the chemical states of Cr in the salt and in the sample at the near-surface region after corrosion. (A,B) BF images showing the corroded alloy and salt with several ROIs highlighted for EELS analysis, with ROIs (a−d) corresponding to the salt regions and ROI (e) to the sample at the near-surface region. (C) EELS spectra from ROIs (a−e). The Cr-$L_{2,3}$ peaks are clearly present in the spectra from ROIs (a−d) in the salt. (D) Relative to references (Cr, $CrCl_2$, and $CrCl_3$), the Cr L_3/L_2 integrated area ratios at ROIs (a−d) were closer to the value of $CrCl_3$ than to Cr^0 or Cr^{2+}, indicating that the main corrosion product was $CrCl_3$.

however, the distribution of Si did not overlap with the salt elements (K, Mg, and Cl) and alloy elements (Ni and Cr). Quartz containers are commonly used by the community to conduct experiments with molten chloride salts. The effects of quartz on corrosion will be future studies.

Apart from the elemental distribution, the chemical (oxidation) state of the Cr in the salt after corrosion was characterized by STEM-EELS. The Cr chemical state was determined based on a comparison of the integrated intensity ratios of the Cr L_3 and L_2 peaks in the EELS spectra from the sample with known references (Cr, $CrCl_2$, and $CrCl_3$), as demonstrated in our prior work.[41] Several regions of interest (ROIs) were selected in the STEM−BF images in Figure 5A−B, including ROIs (a−d) from the salt and ROI (e) in the corroded alloy. The Cr-$L_{2,3}$ peaks (Figure 5C) occurred in ROIs (a−d), while no Cr-$L_{2,3}$ peaks (Figure S9A) were observed at the surface of a grain (ROI (e)). Furthermore, a comparison of the Cr L_3/L_2 integrated area ratio between the ROIs (a−d) and reference compounds is shown in Figure 5D. The values of the Cr L_3/L_2 ratio at ROIs (a−d) were 1.59 ± 0.02, 1.78 ± 0.01, 1.75 ± 0.00, and 1.64 ± 0.03, respectively, which were closer to reference Cr^{3+} at 1.64 ± 0.02 than the reference Cr^{2+} at 2.1 ± 0.02. Although it is possible for both Cr^{2+} and Cr^{3+} to form during reactions according to their redox potentials, the EELS results indicate that $CrCl_3$ was the major stable corrosion product in the salt. Further Cr XANES study will be helpful to understand the chemical and structural evolution of Cr in molten salt or the potential inhomogeneity of Cr species in the salt from the reaction. For Ni, the Ni-$L_{2,3}$ peaks were identified at the surface of the corroded sample ROI (e); at the salt ROIs (a,b and d), Ni peaks were barely detected, while a small Ni L_3 peak was identified in the EELS of the salt region (c), indicating the limited corrosion of Ni into the molten salt (Figure S9B). The presence of Ni without Cr at the grain surface, as shown in the data from ROI (e), was consistent with the finding of a Ni-rich surface layer of corroded Ni−20Cr, as shown in Figure 4A,B.

3.3. Influences of Temperature on Molten Salt Corrosion. In this work, the corrosion of Ni−20Cr in molten KCl−$MgCl_2$ at 600 °C was observed as a two-stage corrosion process. Stage 1 was grain boundary corrosion forming intergranular pores. Stage 2 was surface corrosion on the grains enlarging the intergranular pores. Intergranular corrosion occurred first due to the redox reaction kinetics differences between the grain boundary and the grain, primarily producing Cr ions (Cr^{3+} or Cr^{2+}) in the molten salt. In this study, the influences of Cr^{3+} were discussed further because the STEM/EDS/EELS results showed that it was the primary/stable corrosion product. The STEM/EDS results showed little Ni in the remnant salt. This finding suggests that when Cr atoms at the grain boundary dissolved, the majority of Ni atoms merged to the adjacent grain surface rather than

https://doi.org/10.1021/acsami.2c23207
ACS Appl. Mater. Interfaces 2023, 15, 13772−13782

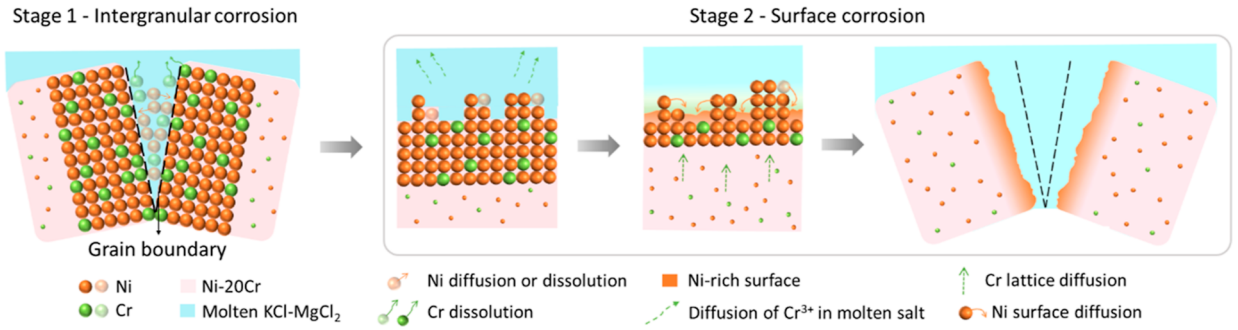

Figure 6. Schematic illustration of the reaction and diffusion behaviors involved in the two-stage corrosion process of Ni−20Cr in molten KCl−$MgCl_2$ at 600 °C. Cr dissolution occurred at the grain boundary first. Then, the Ni atoms diffused to the adjacent grain surface, increasing the proportion of Ni at the grain surface. The Cr atoms at the grain surface further reacted into molten salt; Ni atoms with fast surface diffusion passivated the grain surface, forming a Ni-rich surface. The lattice diffusion of Cr in the alloy was too slow to supply Cr atoms to the grain surface.

dissolving in the molten salt (Figure 6). As the intergranular pores progressed, molten salt filled the pores, creating a liquid−metal interface between the molten salt and the adjacent grains.

Subsequently, during stage 2 of corrosion (Figure 6), Cr dissolution occurred mainly at the surface of the grain without forming pores within them. After corrosion, the grains showed Ni-rich surface layers. After stage 1, the path formed by the voids due to the physical corrosion along grain boundaries was narrow and tortuous in 3D for the molten salt and the dissolved species from the alloy to diffuse through. Considering the Stokes−Einstein relation, tortuous pores reduced the effective diffusion coefficient (D_{eff}) of Cr^{3+} in molten salt.[42] Additionally, Roy et al.[43] revealed that Cr^{3+} species exist in molten KCl−$MgCl_2$ (50−50 mol %) as kinetically stable $[Cr_2Cl_{10}]^{4-}$ clusters and exhibit relatively long lifetimes at the metal−salt interface. The complexation of Cr^{3+} in molten salt could thus further slow the mass transport of Cr^{3+} and the reaction rate of Cr in the grain with molten salt. The above factors could accumulate Cr^{3+} at the metal−salt interface, decreasing the Cr reaction rate according to the Nernst equation if the diffusion of Cr^{3+} and its complex clusters became rate-limited.

Through the other step involved in interfacial processes, the curvature-driven Ni surface diffusion was fast in molten KCl−$MgCl_2$ at 600 °C; these phenomena were observed from the fast flattening of the surface layer and increasing thickness (Figure 2E). When the Cr atoms at the grain surface reacted, the Ni surface diffusion could quickly cover the surface without exposing more Cr atoms underneath, effectively passivating the surfaces of the grains and preventing further rapid corrosion. If percolation dealloying occurred initially during stage 2, nanoscale pores could form within grains. However, as the reaction rate decreased over time, the effect of fast Ni surface diffusion to smoothen the surface could dominate the process. Therefore, planar corrosion into the grains from the grain boundaries occurred without forming percolation pores through dealloying in grains. Additionally, the weight ratio of Cr was potentially below the percolation threshold (~18 wt %) locally because of the diffusion of Ni atoms from the grain boundaries, preventing percolation dealloying from happening.[42] Only the Cr atoms at the surface of the grain reacted, supporting the enrichment of Ni at the grain surface.

However, the surface dealloying of Cr caused a Cr concentration gradient from the center to the surface of the grain, driving the lattice diffusion of Cr. According to the literature, the lattice diffusion coefficient of Cr in Ni-based alloys at 600 °C is in the range of 10^{-22} $m^2 \cdot s^{-1}$.[13] The diffusion distance for Cr via lattice diffusion for 53.2 min (total reaction time) was calculated to be ~0.5 nm, which was too small to supply Cr atoms to the grain surface that would support continuous corrosion. Therefore, the corrosion of the grain could only occur at the grain surface, resulting in the growth of the intergranular pores.

In this study, the behaviors of Ni−20Cr reacting in molten KCl−$MgCl_2$ at 500, 600, 700, and 800 °C were compared to discuss the effects of temperature on the morphological evolution characteristics. Previously published results for samples reacted at 500[19] and 800 °C[16] were reproduced for comparison; the morphological evolution of Ni−20Cr at 700 °C was similar to that at 800 °C and thus is presented in Figure S10. At lower temperatures (500 and 600 °C), intergranular pores formed from a two-stage corrosion mechanism (intergranular and grain surface corrosion). At higher temperatures (700 and 800 °C), a bicontinuous porous structure formed via a percolation dealloying mechanism.

The temperature affected the reaction and transport rates of the various processes in the system; it is primarily the relative rate relationship between the Cr selective dissolution and Ni surface diffusion, resulting in significantly different corrosion processes and morphological evolution characteristics for Ni−20Cr. At lower temperatures, the Cr reaction rate was slow, and the dissolution of Cr formed intergranular pores due to the fast reaction kinetics at the grain boundary. While there occurred surface corrosion of Cr on the grain surfaces, the relatively fast Ni surface diffusion passivated those surfaces. However, at higher temperatures, the Cr reaction rate was relatively fast, leaving less time for the surface diffusion of Ni to passivate the surface. Thus, corrosion followed the percolation dealloying mechanism, forming bicontinuous pores. Further work would be needed to understand the Ni surface diffusion rate and its relationship to Cr dissolution, potentially changing corrosion. By understanding the influences of temperature on molten salt corrosion characteristics, specific corrosion prevention methods, such as adding alloying components or changing the alloy elemental ratio, could be developed based on working temperatures.

4. CONCLUSIONS

In this work, the morphological and chemical changes of Ni−20Cr in molten KCl−$MgCl_2$ (50−50 mol %) at 600 °C were studied by combining multimodal in situ synchrotron trans-

https://doi.org/10.1021/acsami.2c23207
ACS Appl. Mater. Interfaces 2023, 15, 13772−13782

mission X-ray and electron microscopy. The development of the combined multiscale techniques can be applied to study a broader range of functional materials, while their morphological evolution occurs in a liquid medium including chemical reactions in various liquid media and material processing such as crystal growth with fine features in liquid metals.[44] The in situ heating, fast scan acquisition, and nondestructive advantages of synchrotron X-ray nanotomography will be invaluable for time-resolved studies on dynamical and kinetic studies for the synthesis or performance of material applications. A two-stage corrosion process was observed in which the initial pores formed along the grain boundary, followed by corrosion into the adjacent grain surface to increase the pore sizes. In the remnant salt after corrosion, $CrCl_3$ was the main corrosion product. The solubility of $CrCl_3$ and $NiCl_2$ increased with temperature in molten salt. The surface of the corroded alloy was Ni-rich, with the composition of the grain centers remaining as Ni−20Cr. The surface of Ni−20Cr underwent smoothing and coarsening accompanied by a surface flattening and thickness change.

The grain boundary with a higher free energy than the bulk lattice acted as a shortcut for molten salt corrosion at 600 °C. With the Cr atoms dissolved at grain boundaries, Ni atoms or detached Ni-rich particles diffused to the adjacent surface. In the first case, the amount of Cr at the adjacent grain surface was lower than the percolation limit; thus, further corrosion occurred at the grain surface without forming pores within the grain. For corrosion above the percolation limit, the faster Ni surface diffusion rate over the Cr dissolution rate caused Ni to passivate the grain surface.

By comparing the morphological evolution characteristics of Ni−20Cr in molten KCl−$MgCl_2$ from 500 to 800 °C, the effects of temperature on the corrosion were summarized as follows. Intergranular corrosion was prominent at lower temperatures (500−600 °C), while bicontinuous porous structures formed by percolation dealloying were dominant at higher temperatures (700−800 °C). It was hypothesized that the temperature affected the relative rate relationship between Cr dissolution and Ni surface diffusion, determining the morphological evolution characteristics. As different corrosion morphologies have been observed in molten salt applications over a wide range of temperatures, this work explores the fundamental mechanisms of temperature effect which could have impacts on a range of high-temperature molten salt applications.

These mechanistic complexities concerning the temperature-dependent interplay between transport and chemical reactions at the molten salt−metal interfaces are relevant over a broad range of systems and conditions, and they merit much more study. Ongoing research could include whether the presence of particular fission-product metal ions adds mechanistic pathways that produce different corrosion modalities and what effects different base salt compositions have on the balance between modalities. Such studies are essential to reveal the critical mechanisms of molten salt corrosion in nuclear reactors and solar plants and possibly develop case-specific corrosion mitigation methods.

■ ASSOCIATED CONTENT

Supporting Information

The Supporting Information is available free of charge at https://pubs.acs.org/doi/10.1021/acsami.2c23207.

Workflow of image segmentation; surface layer morphological evolution along with reaction time in a local region; thickness determination from the X-ray attenuation change along a line profile across the surface layer; pseudo-XY image showing the pore evolution with the reaction time; two internal regions in Figure 3A; porosity change rate as a function of time at 600 and 800 °C; solubility of $NiCl_2$ and $CrCl_3$ in molten KCl−$MgCl_2$ (50−50 mol %); STEM−BF image of the sample; Si and O STEM/EDS images; EELS spectra of Cr-$L_{2,3}$ edges on ROI (e) in Figure 5B; and corrosion morphological evolution of Ni−20Cr in KCl−$MgCl_2$ at 700 °C (PDF)

Pseudo-cross-sectional images (XY plane) in time series for Ni−20Cr microwire in molten KCl−$MgCl_2$ at 600 °C (AVI)

Pseudo-cross-sectional images (XZ plane) in time series for Ni−20Cr microwire in molten KCl−MgCl2 at 600 °C (AVI)

Morphological evolution of the surface layer as a function of time (AVI)

3D view of the corrosion during stage 1 (MP4)

3D view of the corrosion during stage 2 (MP4)

■ AUTHOR INFORMATION

Corresponding Author

Yu-chen Karen Chen-Wiegart − *Department of Materials Science and Chemical Engineering, Stony Brook University, Stony Brook, New York 11794, United States; National Synchrotron Light Source - II (NSLS-II), Brookhaven National Laboratory, Upton, New York 11973, United States;* orcid.org/0000-0003-4445-2159; Email: Karen.Chen-Wiegart@stonybrook.edu

Authors

Xiaoyang Liu − *Department of Materials Science and Chemical Engineering, Stony Brook University, Stony Brook, New York 11794, United States;* orcid.org/0000-0002-9326-2135

Kaustubh Bawane − *Advanced Characterization Department, Idaho National Laboratory, Idaho Falls, Idaho 83415, United States*

Xiaoyin Zheng − *Department of Materials Science and Chemical Engineering, Stony Brook University, Stony Brook, New York 11794, United States*

Mingyuan Ge − *National Synchrotron Light Source - II (NSLS-II), Brookhaven National Laboratory, Upton, New York 11973, United States;* orcid.org/0000-0001-5682-7443

Phillip Halstenberg − *Department of Chemistry, University of Tennessee, Knoxville, Tennessee 37996, United States;* orcid.org/0000-0002-6030-4503

Dmitry S. Maltsev − *Chemical Sciences Division, Oak Ridge National Laboratory, Oak Ridge, Tennessee 37830, United States;* orcid.org/0000-0001-5678-1465

Alexander S. Ivanov − *Chemical Sciences Division, Oak Ridge National Laboratory, Oak Ridge, Tennessee 37830, United States;* orcid.org/0000-0002-8193-6673

Sheng Dai − *Department of Chemistry, University of Tennessee, Knoxville, Tennessee 37996, United States; Chemical Sciences Division, Oak Ridge National Laboratory, Oak Ridge, Tennessee 37830, United States;* orcid.org/0000-0002-8046-3931

https://doi.org/10.1021/acsami.2c23207
ACS Appl. Mater. Interfaces 2023, 15, 13772−13782

Xianghui Xiao − *National Synchrotron Light Source - II (NSLS-II), Brookhaven National Laboratory, Upton, New York 11973, United States*

Wah-Keat Lee − *National Synchrotron Light Source - II (NSLS-II), Brookhaven National Laboratory, Upton, New York 11973, United States*

Lingfeng He − *Advanced Characterization Department, Idaho National Laboratory, Idaho Falls, Idaho 83415, United States; Department of Nuclear Engineering, North Carolina State University, Raleigh, North Carolina 27695, United States*

Complete contact information is available at: https://pubs.acs.org/10.1021/acsami.2c23207

Notes

The authors declare no competing financial interest.

The digital data for all figures, tables, charts, and any other media contained in this publication and its associated Supporting Information files will be made accessible on the Zenodo repository under Digital Object Identifier (DOI): 10.5281/zenodo.7430671.

■ ACKNOWLEDGMENTS

This work was supported as part of the Molten Salts in Extreme Environments (MSEE) Energy Frontier Research Center, funded by the U.S. Department of Energy, Office of Science, Basic Energy Sciences. BNL, INL, and ORNL are operated under DOE contracts DE-SC0012704, DE-AC07-05ID14517, and DE-AC05-00OR22725, respectively. Work at Stony Brook University was supported by MSEE through a subcontract from BNL. This research used resources, including the Full Field X-ray Imaging (FXI, 18-ID) beamline of the National Synchrotron Light Source II and a U.S. Department of Energy (DOE) Office of Science User Facility operated for the DOE Office of Science by Brookhaven National Laboratory under Contract DE-SC0012704. The authors are grateful to Arthur Ronne and Lin-Chieh Yu for their help with the sample preparation. The following present and former Chen-Wiegart group members are acknowledged for conducting beamtime experiments: Cheng-Hung Lin, Chonghang Zhao, Qingkun Meng, and Dean Yen.

■ REFERENCES

(1) Guo, S. Q.; Zhang, J. S.; Wu, W.; Zhou, W. T. Corrosion in the Molten Fluoride and Chloride Salts and Materials Development for Nuclear Applications. *Prog. Mater. Sci.* **2018**, *97*, 448−487.

(2) Serp, J.; Allibert, M.; Beneš, O.; Delpech, S.; Feynberg, O.; Ghetta, V.; Heuer, D.; Holcomb, D.; Ignatiev, V.; Kloosterman, J. L.; Luzzi, L.; Merle-Lucotte, E.; Uhlíř, J.; Yoshioka, R.; Zhimin, Z. M. The Molten Salt Reactor (Msr) in Generation Iv: Overview and Perspectives. *Prog. Nucl. Energy* **2014**, *77*, 308−319.

(3) Zhou, W. Y.; Yang, Y.; Zheng, G. Q.; Woller, K. B.; Stahle, P. W.; Minor, A. M.; Short, M. P. Proton Irradiation-Decelerated Intergranular Corrosion of Ni-Cr Alloys in Molten Salt. *Nat. Commun.* **2020**, *11*, 3430.

(4) Gomez-Vidal, J. C.; Tirawat, R. Corrosion of Alloys in a Chloride Molten Salt (Nacl-Licl) for Solar Thermal Technologies. *Sol. Energy Mater. Sol. Cells* **2016**, *157*, 234−244.

(5) Raiman, S. S.; Lee, S. Aggregation and Data Analysis of Corrosion Studies in Molten Chloride and Fluoride Salts. *J. Nucl. Mater.* **2018**, *511*, 523−535.

(6) Sun, H.; Wang, J. Q.; Tang, Z. F.; Liu, Y. Y.; Wang, C. Y. Assessment of Effects of Mg Treatment on Corrosivity of Molten Nacl-Kclmgcl2 Salt with Raman and Infrared Spectra. *Corros. Sci.* **2020**, *164*, 108350.

(7) Zhao, Y. Y.; Klammer, N.; Vidal, J. Purification Strategy and Effect of Impurities on Corrosivity of Dehydrated Carnallite for Thermal Solar Applications. *Rsc Advances* **2019**, *9*, 41664−41671.

(8) Wang, Y. L.; Zeng, C. L.; Li, W. H. The Influence of Temperature Gradient on the Corrosion of Materials in Molten Fluorides. *Corros. Sci.* **2018**, *136*, 180−187.

(9) Kurley, J. M.; Halstenberg, P. W.; McAlister, A.; Raiman, S.; Dai, S.; Mayes, R. T. Enabling Chloride Salts for Thermal Energy Storage: Implications of Salt Purity. *Rsc Advances* **2019**, *9*, 25602−25608.

(10) Wang, Y. L.; Wang, Q.; Liu, H. J.; Zeng, C. L. Effects of the Oxidants H2o and Crf3 on the Corrosion of Pure Metals in Molten (Li,Na,K)F. *Corros. Sci.* **2016**, *103*, 268−282.

(11) Bell, S.; Steinberg, T.; Will, G. Corrosion Mechanisms in Molten Salt Thermal Energy Storage for Concentrating Solar Power. *Renewable Sustainable Energy Rev.* **2019**, *114*, 109328.

(12) Ding, W. J.; Bonk, A.; Bauer, T. Corrosion Behavior of Metallic Alloys in Molten Chloride Salts for Thermal Energy Storage in Concentrated Solar Power Plants: A Review. *Front. Chem. Sci. Eng.* **2018**, *12*, 564−576.

(13) Sun, H.; Zhang, P.; Wang, J. Q. Effects of Alloying Elements on the Corrosion Behavior of Ni-Based Alloys in Molten Nacl-Kcl-Mgcl(2)Salt at Different Temperatures. *Corros. Sci.* **2018**, *143*, 187−199.

(14) Hofmeister, M.; Klein, L.; Miran, H.; Rettig, R.; Virtanen, S.; Singer, R. F. Corrosion Behaviour of Stainless Steels and a Single Crystal Superalloy in a Ternary Licl-Kcl-Cscl Molten Salt. *Corros. Sci.* **2015**, *90*, 46−53.

(15) Gill, S. K.; Sure, J.; Wang, Y. C.; Layne, B.; He, L. F.; Mahurin, S.; Wishart, J. F.; Sasaki, K. Investigating Corrosion Behavior of Ni and Ni-20cr in Molten Zncl2. *Corros. Sci.* **2021**, *179*, 109105.

(16) Liu, X. Y.; Ronne, A.; Yu, L. C.; Liu, Y.; Ge, M. Y.; Lin, C. H.; Layne, B.; Halstenberg, P.; Maltsev, D. S.; Ivanov, A. S.; Antonelli, S.; Dai, S.; Lee, W. K.; Mahurin, S. M.; Frenkel, A. I.; Wishart, J. F.; Xiao, X. H.; Chen-Wiegart, Y. Formation of Three-Dimensional Bicontinuous Structures Via Molten Salt Dealloying Studied in Real-Time by in Situ Synchrotron X-Ray Nano-Tomography. *Nat. Commun.* **2021**, *12*, 3441.

(17) Ronne, A.; He, L. F.; Dolzhnikov, D.; Xie, Y.; Ge, M. Y.; Halstenberg, P.; Wang, Y. C.; Manard, B. T.; Xiao, X. H.; Lee, W. K.; Sasaki, K.; Dai, S.; Mahurin, S. M.; Chen-Wiegart, Y. C. K. Revealing 3d Morphological and Chemical Evolution Mechanisms of Metals in Molten Salt by Multimodal Microscopy. *ACS Appl. Mater. Interfaces* **2020**, *12*, 17321−17333.

(18) Yang, Y.; Zhou, W.; Yin, S.; Wang, S.; Yu, Q.; Olszta, M.; Zhang, Y.-Q.; Zeltmann, S.; Li, M.; Jin, M.; Schreiber, D.; Ciston, J.; Scott, M. C.; Scully, J.; Ritchie, R.; Asta, M.; Li, J.; Short, M.; Minor, A. One Dimensional Wormhole Corrosion in Metals. *Nat. Commun.* **2023**, *14*, 988.

(19) Bawane, K.; Liu, X. Y.; Gakhar, R.; Woods, M.; Ge, M. Y.; Xiao, X. H.; Lee, W. K.; Halstenberg, P.; Dai, S.; Mahurin, S.; Pimblott, S. M.; Wishart, J. F.; Chen-Wiegart, Y. C. K.; He, L. F. Visualizing Time-Dependent Microstructural and Chemical Evolution During Molten Salt Corrosion of Ni-20cr Model Alloy Using Correlative Quasi in Situ Tem and in Situ Synchrotron X-Ray Nano-Tomography. *Corros. Sci.* **2022**, *195*, 109962.

(20) Halstenberg, P. W.; Maltsev, D.; Nguyen, D.; Kim, E.; Dai, S. Mechanochemical Synthesis of High-Purity Anhydrous Binary Alkali and Alkaline Earth Chloride Mixtures. *Ind. Eng. Chem. Res.* **2020**, *59*, 19884−19889.

(21) Dolzhnikov, D.; Dai, S. *M4ft 18or110102182-Develop a New Composite Molten Salt Fluid Exhibiting an Increased Heat Capacity of 10%*; Oak Ridge National Laboratory, 2018.

(22) Wu, F.; Roy, S.; Ivanov, A. S.; Gill, S. K.; Topsakal, M.; Dooryhee, E.; Abeykoon, M.; Kwon, G.; Gallington, L. C.; Halstenberg, P.; Layne, B.; Ishii, Y.; Mahurin, S. M.; Dai, S.; Bryantsev, V. S.; Margulis, C. J. Elucidating Ionic Correlations Beyond

Simple Charge Alternation in Molten MgCl2-KCl Mixtures. *J. Phys. Chem. Lett.* **2019**, *10*, 7603−7610.
(23) Ge, M. Y.; Coburn, D. S.; Nazaretski, E.; Xu, W. H.; Gofron, K.; Xu, H. J.; Yin, Z. J.; Lee, W. K. One-Minute Nano-Tomography Using Hard X-Ray Full-Field Transmission Microscope. *Appl. Phys. Lett.* **2018**, *113*, 083109.
(24) Antonelli, S.; Ronne, A.; Han, I.; Ge, M. Y.; Layne, B.; Shahani, A. J.; Iwamatsu, K.; Wishart, J. F.; Hulbert, S. L.; Lee, W. K.; Chen-Wiegart, Y. C. K.; Xiao, X. H. Versatile Compact Heater Design for in Situ Nano-Tomography by Transmission X-Ray Microscopy. *J. Synchrotron Radiat.* **2020**, *27*, 746−752.
(25) Ge, M. Y.; Lee, W. K. Pyxas - an Open-Source Package for 2d X-Ray near-Edge Spectroscopy Analysis. *J. Synchrotron Radiat.* **2020**, *27*, 567−575.
(26) Ravel, B.; Newville, M. ATHENA,ARTEMIS,HEPHAESTUS: data analysis for X-ray absorption spectroscopy usingIFEFFIT. *J. Synchrotron Radiat.* **2005**, *12*, 537−541.
(27) Gürsoy, D.; De Carlo, F.; Xiao, X. H.; Jacobsen, C. TomoPy: a framework for the analysis of synchrotron tomographic data. *J. Synchrotron Radiat.* **2014**, *21*, 1188−1193.
(28) Dowd, B. A.; Campbell, G. H.; Marr, R. B.; Nagarkar, V.; Tipnis, S.; Axe, L.; Siddons, D. P. Developments In Synchrotron X-Ray Computed Microtomography at the National Synchrotron Light Source, *Conference on Developments in X-Ray Tomography II*, Denver, Co, July 22-23, 1999; pp 224-236.
(29) Arganda-Carreras, I.; Kaynig, V.; Rueden, C.; Eliceiri, K. W.; Schindelin, J.; Cardona, A.; Sebastian Seung, H. S. Trainable Weka Segmentation: A Machine Learning Tool for Microscopy Pixel Classification. *Bioinformatics* **2017**, *33*, 2424−2426.
(30) Virtanen, P.; Gommers, R.; Oliphant, T. E.; Haberland, M.; Reddy, T.; Cournapeau, D.; Burovski, E.; Peterson, P.; Weckesser, W.; Bright, J.; van der Walt, S. J.; Brett, M.; Wilson, J.; Millman, K. J.; Mayorov, N.; Nelson, A. R. J.; Jones, E.; Kern, R.; Larson, E.; Carey, C. J.; Polat, I.; Feng, Y.; Moore, E. W.; VanderPlas, J.; Laxalde, D.; Perktold, J.; Cimrman, R.; Henriksen, I.; Quintero, E. A.; Harris, C. R.; Archibald, A. M.; Ribeiro, A. N. H.; Pedregosa, F.; van Mulbregt, P.; Vijaykumar, C.; Bardelli, A. P.; Rothberg, A.; Hilboll, A.; Kloeckner, A.; Scopatz, A.; Lee, A.; Rokem, A.; Woods, C. N.; Fulton, C.; Masson, C.; Häggström, C.; Fitzgerald, C.; Nicholson, D. A.; Hagen, D. R.; Pasechnik, D. V.; Olivetti, E.; Martin, E.; Wieser, E.; Silva, F.; Lenders, F.; Wilhelm, F.; Young, G.; Price, G. A.; Ingold, G.-L.; Allen, G. E.; Lee, G. R.; Audren, H.; Probst, I.; Dietrich, J. P.; Silterra, J.; Webber, J. T.; Slavič, J.; Nothman, J.; Buchner, J.; Kulick, J.; Schönberger, J. L.; de Miranda Cardoso, J. V.; Reimer, J.; Harrington, J.; Rodríguez, J. L. C.; Nunez-Iglesias, J.; Kuczynski, J.; Tritz, K.; Thoma, M.; Newville, M.; Kümmerer, M.; Bolingbroke, M.; Tartre, M.; Pak, M.; Smith, N. J.; Nowaczyk, N.; Shebanov, N.; Pavlyk, O.; Brodtkorb, P. A.; Lee, P.; McGibbon, R. T.; Feldbauer, R.; Lewis, S.; Tygier, S.; Sievert, S.; Vigna, S.; Peterson, S.; More, S.; Pudlik, T.; Oshima, T.; Pingel, T. J.; Robitaille, T. P.; Spura, T.; Jones, T. R.; Cera, T.; Leslie, T.; Zito, T.; Krauss, T.; Upadhyay, U.; Halchenko, Y. O.; Vázquez-Baeza, Y. Scipy 1.0: Fundamental Algorithms for Scientific Computing in Python. *Nat. Methods* **2020**, *17*, 261−272.
(31) Zhang, M. Y.; Ge, J. B.; Yin, T. Q.; Zhang, J. S. Redox Potential Measurements of Cr(Ii)/Cr Ni(Ii)/Ni and Mg(Ii)/Mg in Molten Mgcl2-Kcl-Nacl Mixture. *J. Electrochem. Soc.* **2020**, *167* (11), 116505.
(32) RobertBalluffi, W. S. M. A.; Craig Carter, W. *Kinetics of Materials*; Wiley, 2005.
(33) Liu, X.; Ronne, A.; Yu, L.-C.; Halstenberg, P.; Xiao, X.; Lee, W.-K.; Dai, S.; Ge, M.; Chen-Wiegart, Y.-c. K. Heterogeneous 3d Morphological Evolution of Ni Microparticles in Molten Salts: Visualized by Operando Synchrotron X-Ray Nano-Tomography. *JOM* **2023**, DOI: 10.1007/s11837-023-05715-8.
(34) Liu, Y. J.; Meirer, F.; Williams, P. A.; Wang, J. Y.; Andrews, J. C.; Pianetta, P. Txm-Wizard: A Program for Advanced Data Collection and Evaluation in Full-Field Transmission X-Ray Microscopy. *J. Synchrotron Radiat.* **2012**, *19*, 281−287.
(35) Lin, F.; Nordlund, D.; Markus, I. M.; Weng, T. C.; Xin, H. L.; Doeff, M. M. Profiling the Nanoscale Gradient in Stoichiometric Layered Cathode Particles for Lithium-Ion Batteries. *Energy Environ. Sci.* **2014**, *7*, 3077−3085.
(36) Qian, G. N.; Wang, J. Y.; Li, H.; Ma, Z. F.; Pianetta, P.; Li, L. S.; Yu, X. Q.; Liu, Y. J. Structural and Chemical Evolution in Layered Oxide Cathodes of Lithium-Ion Batteries Revealed by Synchrotron Techniques. *Natl. Sci. Rev.* **2022**, *9* (2), nwab146.
(37) Badwe, N.; Chen, X.; Schreiber, D. K.; Olszta, M. J.; Overman, N. R.; Karasz, E. K.; Tse, A. Y.; Bruemmer, S. M.; Sieradzki, K. Decoupling the Role of Stress and Corrosion in the Intergranular Cracking of Noble-Metal Alloys. *Nat. Mater.* **2018**, *17*, 887−893.
(38) Rohrer, G. S. Grain Boundary Energy Anisotropy: A Review. *J. Mater. Sci.* **2011**, *46*, 5881−5895.
(39) Kumar, S.; Todd, A. 12 - Corrosion in Molten Salts. In *Molten Salts Chemistry*; Elsevier, 2013, pp 241−267.
(40) Chen, Q.; Sieradzki, K. Mechanisms and Morphology Evolution in Dealloying. *J. Electrochem. Soc.* **2013**, *160*, C226−C231.
(41) Bawane, K.; Manganaris, P.; Wang, Y.; Sure, J.; Ronne, A.; Halstenberg, P.; Dai, S.; Gill, S.; Sasaki, K.; Chen-Wiegart, Y.-c. K.; Gakhar, R.; Mahurin, S.; Pimblott, S.; Wishart, J.; He, L. Determine Oxidation State of Transition Metals in Molten Salt Corrosion Using Electron Energy Loss Spectroscopy. *Scr. Mater.* **2021**, *197*, 113790.
(42) Chen-Wiegart, Y. C. K.; DeMike, R.; Erdonmez, C.; Thornton, K.; Barnett, S. A.; Wang, J. Tortuosity Characterization of 3d Microstructure at Nano-Scale for Energy Storage and Conversion Materials. *J. Power Sources* **2014**, *249*, 349−356.
(43) Roy, S.; Sharma, S.; Karunaratne, W. V.; Wu, F.; Gakhar, R.; Maltsev, D. S.; Halstenberg, P.; Abeykoon, M.; Gill, S. K.; Zhang, Y. P.; Mahurin, S. M.; Dai, S.; Bryantsev, V. S.; Margulis, C. J.; Ivanov, A. S. X-Ray Scattering Reveals Ion Clustering of Dilute Chromium Species in Molten Chloride Medium. *Chem. Sci.* **2021**, *12*, 8026.
(44) Idrus-Saidi, S. A.; Tang, J. B.; Lambie, S.; Han, J. L.; Mayyas, M.; Ghasemian, M. B.; Allioux, F. M.; Cai, S. X.; Koshy, P.; Mostaghimi, P.; Steenbergen, K. G.; Barnard, A. S.; Daeneke, T.; Gaston, N.; Kalantar-Zadeh, K. Liquid Metal Synthesis Solvents for Metallic Crystals. *Science* **2022**, *378*, 1118−1124.